Neutral Stability, Rate Propagation, and Critical Branching in Feedforward Networks

N. Alex Cayco-Gajic
caycogajic@gmail.com
Department of Applied Mathematics, University of Washington, Seattle,
WA 98195, U.S.A.

Eric Shea-Brown
etsb@washington.edu
Departments of Applied Mathematics and of Physiology and Biophysics
and Program in Neurobiology and Behavior, University of Washington,
Seattle, WA 98195, U.S.A.

Recent experimental and computational evidence suggests that several dynamical properties may characterize the operating point of functioning neural networks: critical branching, neutral stability, and production of a wide range of firing patterns. We seek the simplest setting in which these properties emerge, clarifying their origin and relationship in random, feedforward networks of McCullochs-Pitts neurons. Two key parameters are the thresholds at which neurons fire spikes and the overall level of feedforward connectivity. When neurons have low thresholds, we show that there is always a connectivity for which the properties in question all occur, that is, these networks preserve overall firing rates from layer to layer and produce broad distributions of activity in each layer. This fails to occur, however, when neurons have high thresholds. A key tool in explaining this difference is the eigenstructure of the resulting mean-field Markov chain, as this reveals which activity modes will be preserved from layer to layer. We extend our analysis from purely excitatory networks to more complex models that include inhibition and local noise, and find that both of these features extend the parameter ranges over which networks produce the properties of interest.

1 Introduction

Many basic questions remain unresolved in understanding how simple features of network connectivity determine the statistical structure of their outputs. In particular, as we vary the average connectivity strength between model neurons, what kinds of transitions occur in model dynamics? The first dynamical property we might study at a transition is neutral stability of trajectories. Intuitively, it appears that neutral stability could favor signal

transmission, because it suggests that input patterns (and their noisy perturbations) will retain their original separation in state space, neither diverging nor converging toward some fixed attractor (Bertschinger & Natschlager, 2004; Legenstein & Maass, 2007). The second, allied property that could occur as networks transition from weak to strong connectivity is the production of a wide range of output states—that is, a mix of firing patterns that induce a broad distribution with high response entropy. If responses are tallied by total network output, this could require statistical correlations of all orders (Amari, Nakahara, Wu, & Sakai, 2003); thus, higher-order correlations are another statistical property of interest at network transitions. Finally, an assay that involves all of these properties is the decodability of input patterns based on network outputs.

But how are all of these properties related? Do networks ever exhibit all of them simultaneously, and if so, when? Developing the complete picture is a formidable challenge; in this letter, we progress by answering these questions in what is probably the most tractable class of systems in which they can be studied: noisy, feedforward networks of thresholding neurons (Nowotny and Huerta, 2003).

Several prior studies of signal propagation in feedforward networks inform our approach. These suggest that a wide range of network responses fails to occur in broad parameter regimes: rather, the only outputs produced are all cells firing or being silent simultaneously. This is due to the buildup of correlations among neural activity at each layer, even when inputs drive the cells to fire independently in the first layer. In particular, for iteratively constructed in vitro feedforward networks, neurons displayed a marked tendency to synchronize (Reyes, 2003). Subsequent simulations and analyses with thresholding neurons have corroborated these findings, arguing that any initial spike count distribution becomes strongly bimodal after a few layers (Nowotny & Huerta, 2003). Integrate-and-fire neurons similarly fail to transmit activity without decaying or saturating to a point independent of the input rate but are able to support stable propagation of highly synchronized volleys of spikes even in the presence of asynchronous background noise with low firing rates (Diesmann, Gewaltig, & Aertsen, 1999; Kumar, Rotter, & Aertsen, 2008; Litvak, Sompolinsky, Segev, & Abeles, 2003; Tetzlaff, Geisel, & Diesmann, 2002). These cascades of coherent activity, called synfire chains, have been observed experimentally and are hypothesized to encode stimuli through precise spatiotemporal spike timing (Abeles, Bergman, Margalit, & Vaadia, 1993). However, in embedded feedforward networks, even synchronous propagation dies out if background network activity is sufficiently synchronous or has a high firing rate (Kumar et al., 2008). If synapses are strengthened and connectivity sparse, rate propagation but not synfire activity can be sustained (Vogels & Abbott, 2005). Moreover, different studies demonstrate a critical regime with broadly distributed output patterns and significant higher-order interactions (Beggs & Plenz, 2003; Yu et al., 2011).

As we will further explore here, the key difference among these studies is the threshold number of excitatory inputs that each cell must receive in order to fire (Kumar, Rotter, & Aertsen, 2010). This threshold is low in the work of Beggs and Plenz (2003) (a single spike) and Vogels and Abbott (2005) but much higher for Nowotny and Huerta (2003), Reyes (2003), and Litvak et al. (2003). As reviewed in Kumar et al. (2010), densely connected feedforward networks with synapses that are weak relative to threshold tend to produce more synchrony than their sparsely connected counterparts due to the neurons having more shared inputs (Rosenbaum, Trousdale, & Josic, 2010). Thus, as synaptic inputs are weak compared to spike thresholds in many biological settings, it may appear that synchrony is inevitable. However, noise local to each neuron decreases synchrony and can do so without damaging the capacity to transmit signals, at least those defined by firing rates within each network layer (van Rossum, Turrigiano, & Nelson, 2002, but see also Nowotny & Huerta, 2003; Reyes, 2003).

Here, we undertake to unify these results through a common mathematical framework and extend them by treating multiple assays of network outputs. In particular, we show when and how neutral stability, broad response distributions, higher-order correlations, and the transmission of firing rate signals coexist and when these properties fail to coexist. For any level of spike threshold, we find that there is always an intermediate value of network connectivity characterized by neutral stability and higher-order correlations. High response entropy and transmission of firing rates, however, occur only at this point when neurons have low thresholds or added noise.

The narrative of the letter proceeds as follows. Section 2 gives the setup of the model. In section 3, we introduce the branching ratio, describing how layer-averaged activity—that is, firing rates—is propagated from layer to layer. Next, in section 4, we develop tools that give a more refined view of how activity is transmitted. Specifically, we show that the model can be reduced to a mean-field Markov chain and that the eigenstructure of the corresponding transition matrix reveals intermediate parameter values for which the networks support persistent, broadly distributed responses. In section 5, we study the resulting responses in terms of higher-order correlations and response entropy, showing that both are maximized at this intermediate parameter regime. Section 6 introduces a combined metric, which assesses the capacity of networks to preserve rates from one layer to the next while maintaining broadly distributed responses. In sections 7 and 8, we apply the same analyses to excitatory-inhibitory networks and to those with localized background noise, and we see that both factors increase parameter ranges over which the propagation of broad activity distributions with preserved firing rates occurs.
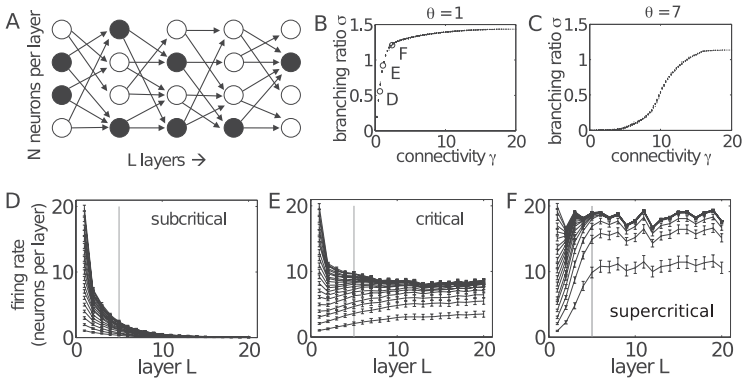
Figure 1: Average rate transmission in feedforward networks. (A) Schematic of a feedforward network. Filled circles indicate spikes, hollow circles quiescence (i.e., absence of firing). In this example, $N = 4$, $L = 5$, $C = 2$, $p = 0.5$, and $\theta = 1$. (B, C) Branching ratio σ as a function of connectivity strength γ for $N = 20$, (B) $\theta = 1$, and (C) $\theta = 7$. Each data point is the branching ratio of a network of a particular connectivity structure. (D–F) Simulated propagation of firing rates shown for three sample networks with $\theta = 1$ and $C = 3$, $p = 0.25$, 0.43, 0.85, respectively. These parameters are also indicated by the markers in panel B. Noisy, uncorrelated input is injected into the first layer, and the resulting firing rates are averaged over 1000 trials plotted over multiple layers. Error bars indicate standard deviation scaled by a factor of $1/10$ to facilitate comparison. Vertical gray bars are shown at $L = 5$ to emphasize that henceforth we will primarily be concerned with shallow layers. (D) In subcritical networks ($\sigma < 1$), activity tends to die out. (F) In supercritical ($\sigma > 1$) networks, activity saturates. (E) Critical networks ($\sigma \approx 1$) reveal the greatest fidelity in propagating Poisson input rates through layers; however, while this picture is qualitatively true for networks of low-threshold neurons, when θ reaches higher values, networks tend to transmit only high or low rates (see section 6).

2 Model of Stochastic Feedforward Networks

2.1 Network. Following Nowotny and Huerta (2003), we examine a network of binary (McCulloch & Pitts, 1943) neurons in a feedforward architecture with probabilistic synapses and input (see Figure 1A for a schematic). Each layer consists of N identical neurons. In general, we will illustrate $N = 20$; results hold for larger N as well, as we summarize in section 9. The neurons are thresholding units that spike if they receive at least θ synaptic inputs from neurons in the previous layer and are otherwise quiescent (i.e., silent). The connectivity structure between layers is random and spatially homogenous; each neuron upstream is connected to C postsynaptic neurons chosen uniformly from the downstream layer. Connections

between neurons have a fixed probability p of synaptic transmission. In this letter, we are interested in signal propagation through a fixed number of layers, as we expect biological feedforward networks to be shallow (we will in general take $L = 5$). The number of layers through which a rate signal can be transmitted in similar feedforward networks before losing information has been addressed by Toyoizumi (2012), Lim and Goldman (2012), and Ganguli, Huh, and Sompolinsky (2008).

We concentrate solely on networks with a feedforward connectivity structure. However, these networks are equivalent to synchronously updated, discrete-time systems with random recurrent connections (including "autapse" connections to and from cells to themselves), under the annealing approximation (Bertschinger & Natschlager, 2004). Thus, to the extent that these assumptions hold, the results of this letter may also be applied to the evaluation of persistent activity in recurrent networks.

2.2 Stimuli. The networks are driven by a stimulus to elicit an average spike count of $S \in \{0, \ldots N\}$ firing neurons in the first layer at that time step. Unless otherwise specified, this stochastic input is injected independently so that each neuron in the first layer responds as an independent (0,1) Bernoulli random variable with biased probability S/N of spiking (taking value 1). This results in a binomially distributed spike count in the first layer.

2.3 Propagation. The state of the Lth layer is denoted by $\mathbf{x}_L$, an N-vector of zeros and ones, and the connectivity matrix between layers L and $L + 1$ by E_L. (Henceforth we will use E to refer to the $N \times N \times L - 1$ connectivity tensor of the entire network.) Since the connections between neurons are stochastic, each synapse in a given trial fails with probability $1 - p$. It will be useful to call the realization of E_L according to the probability of synaptic transmission the "effective" connectivity matrix $\hat{E}_L$, keeping in mind that different trials will yield different $\hat{E}_L$ yet E_L will remain fixed. The state at layer L of a realization of a given network can now be expressed as

$$\mathbf{x}_{L+1} = \Theta\big(\hat{E}_L \mathbf{x}_L - \theta\big), \tag{2.1}$$

where Θ is the elementwise Heaviside step function. The key parameter in this system is the connectivity strength $\gamma = Cp$.

2.4 Limitations and Simplifications. We note several important facts about the model setup and analysis. First, this model has no time explicit in its dynamics; each trial can be thought of as a wave of activity evolving from a particular initialization in the first layer and is independent of the next. Because of this, the phenomenon of synchrony in the usual temporal sense is not applicable. The corresponding concept of synchrony is when

neurons in a layer tend to fire, or be quiescent, together in a given trial; this is what we will mean in the remainder of this letter when we refer to synchrony or synchronous coding. Second, because of the assumption of spatial homogeneity in both inputs and network architecture, this model is not well suited to study spatial modes of activity.

Third, and most important, our analysis henceforth focuses on the total activity within each layer. That is, rather than quantify network responses in the full space of 2^N firing patterns that can occur in each layer, we restrict our description to the number of cells that fire in that layer: the $N+1$ different values of the (layer-averaged) firing rate.

3 The Branching Ratio

To understand the qualitative dynamics and average firing rate transmission through multiple layers, we borrow a useful tool from the criticality literature (Beggs & Plenz, 2003). A critical transition regime is often experimentally defined by the branching ratio σ, the ratio between the number of cells in a population firing at a particular time step and the number of cells firing at the previous time step, averaged over time. To avoid decay or growth of activity, the system must produce firing rate dynamics that are neutrally stable, satisfying $\sigma \approx 1$; such networks are labeled critical.

In our feedforward framework, the relevant measurement is the branching ratio averaged over trials and layers rather than time. To quantify the general capacity of a particular network with fixed connectivity structure E to maintain activity in a one-to-one manner, we will also average this layerwise branching ratio over repeated trials with the same network, each with different stimulus rates as well as different (random) inputs $\mathbf{x}_1$ to the first layer. The result is

$$\sigma = \left\langle \left\langle \left\langle \frac{S_L}{S_{L-1}} \right\rangle_L \right\rangle_{\hat{E}, \mathbf{x}_1} \right\rangle_S, \tag{3.1}$$

where S_L is the number of neurons spiking in layer L on a given trial. Throughout this letter, when we refer to the branching ratio, we mean σ.

We conducted Monte Carlo simulations to compute how this quantity changes with connectivity level γ. In detail, at a fixed γ, we first chose one example of a network structure E for every $C \geq \lceil \gamma \rceil$, the constrained value ensuring that $p < 1$. For each E, we then input a deterministic rate of exactly $S = \theta + 1, \ldots, N$ spiking neurons in the first layer with 100 random instantiations of $\mathbf{x}_1$, evolve the network, and measure the ratios S_L/S_{L-1} for each layer until either the neural activity dies out or the last layer is reached. Finally, σ is computed as the average over the 100 random network realizations and instantiations at the first layer, and subsequently over all

stimulus levels greater than θ spiking neurons per layer (as any input less than that is guaranteed to be extinguished at the next layer).

Figures 1B and 1C show results over five layers. Each of the tight scatter of points at each value of connectivity γ is the branching ratio of a particular network with that value of connectivity and a specific architecture E. (The fact that there is very little variation at a given level γ supports our choice of this combined parameter as the principal one in our study.[1]) Note that as we sweep connectivity γ from small to large values, we pass through a critical value (which we shall denote by γ_{obs}) at which $\sigma \approx 1$. Thus, we find that the transition (critical) branching parameter is consistently found in our networks at some intermediate connectivity level.

We next illustrate the implications of the branching parameter for propagation of firing rates across network layers. For many different networks, we compute rate trajectories averaged over 1000 trials for input rates ranging from 0 to $N = 20$ neurons firing in the first layer. In each trial, S and E are fixed, yet $\mathbf{x}_1$ and $\hat{E}$ change probabilistically. The evolution of the firing rate over 20 layers is shown for three representative networks with threshold $\theta = 1$ in Figures 1D to 1F. In subcritical networks (see Figure 1D), neural activity dies after a few layers regardless of stimulus. The supercritical, $\sigma > 1$, network (see Figure 1F) inflates rates to nearly maximal values, and as in the subcritical case, it is difficult to distinguish between two inputs based on output rate alone. In critical networks, however, rate trajectories remain separated at each layer (see Figure 1E). This result is in agreement with other findings in the literature regarding information transmission of critical networks. Overall, these simulations confirm the expected picture that the average firing rate statistic is best propagated through networks when $\sigma \approx 1$.

Beyond preservation of firing rates from one layer to the next, we are interested in networks that can produce a broad distribution of responses and avoid the limitations of strong synchrony. To assess this, in the next section we introduce a tool to describe propagation of firing rate distributions across layers via a mean-field approximation.

4 Mean-Field Markov Chain Model and Spectral Analysis

Since the state of each layer depends solely on the state of the previous layer and the synaptic connections between layers, our feedforward networks are Markov chains (Nowotny & Huerta, 2003). Furthermore, as we aim

---

[1]In the following sections we reduce the two parameters C and p dictating network connectivity to the single connectivity parameter γ; this is supported by the observation that variation in σ for fixed γ but varying values of C and p is has a negligible impact on the branching ratio, as shown by the tight scatter of points at each γ in Figures 1B and 1C. Moreover, in the mean-field theory we develop, it is also the case that γ, rather than C and p separately, enters.

to describe only the propagation of layer-averaged firing rates rather than particular firing patterns (or binary words), our Markov chain has $N + 1$ states. We proceed to derive a mean-field description of the Markov chain for each connectivity level γ by averaging over possible connection matrices, yielding a discrete-time dynamical system describing the evolution of the spike counts or firing rate from layer to layer. To do this, we make two assumptions: conditional independence and permutation symmetry. The former assumes that neurons in the downstream layer are conditionally independent given the number of neurons firing in the previous layer. This condition effectively ignores correlations that would arise due to inhomogeneous connectivity architectures (e.g., divergent motifs). However, conditional independence neither implies nor is implied by unconditional independence; therefore, activity between neurons may still be correlated ultimately.

The second assumption states that neurons within a layer are permutation symmetric, meaning that each group of k neurons in a layer has the same statistical properties. Both approximations (and therefore the mean-field model) are exact in the special case of all-to-all connectivity ($C = N$), for which Nowotny and Huerta (2003) developed the same description. When $C < N$, the mean-field and true models differ; the latter would be obtained by first finding the spike count distributions for fixed connectivity and then averaging over all E. However, for the excitatory networks considered in the main part of the letter (sections 2–6), we have verified numerically that the mean-field model is a good predictor of the true spike count dynamics except in the limit of large p and small C (see appendix C).

The mean-field transition matrix A—the matrix whose (n, m)th element is the probability that there are $S_L = m$ neurons spiking at a layer given $S_{L-1} = n$ spiking in the previous layer—is given by

$$A_{nm} = \binom{N}{m} q_n^m (1 - q_n)^{N-m} \tag{4.1}$$

if $n \geq \theta$. Here, q_n is the probability that a downstream neuron will fire assuming n spiking neurons in the previous layer:

$$q_n = \sum_{k=\theta}^{n} \binom{n}{k} \left(\frac{\gamma}{N}\right)^k \left(1 - \frac{\gamma}{N}\right)^{n-k}. \tag{4.2}$$

If $n < \theta$, then $q_n = 0$ and $A_{nm} = 0$. In principle, A could be derived from the transition matrix of the original Markov chain (see appendix B for details).

When we use the transition matrix, the spike count probability distribution P_L at layer L (the vector of length $N + 1$ whose jth component is the probability that j neurons are firing in layer L) is simply given by matrix-vector multiplication: $P_L = P_{L-1}A$.

The long-term behavior of these feedforward networks can be predicted using the eigenvalues and eigenvectors of the mean-field transition matrix. To illustrate this, assume A is diagonalizable, so that the input probability distribution $P_{\text{input}} = P_1$ can be decomposed into a linear combination of the eigenvectors of A:

$$P_{\text{input}} = \alpha_0 v_0 + \alpha_1 v_1 + \cdots + \alpha_N v_N.$$

The spike count probability distribution at the Lth layer is simply $P_L = P_{\text{input}} A^L$:

$$P_L = \alpha_0 \lambda^L v_0 + \alpha_1 \lambda_1^L v_1 + \cdots + \alpha_N \lambda_N^L v_N.$$

The persistence of different eigenmodes through layers is determined by the size of their corresponding eigenvalues.[2] If $\lambda_i \ll 1$, then after a few layers, the contribution of the ith eigenmode will decay to become negligible. On the other hand, eigenmodes whose eigenvalues are near 1 will survive through many layers.

We analyze the eigenstructure of A through a combination of mathematical analysis and computational argument. First, it can be proven that A has one unique stationary state corresponding to all neurons being quiescent: $v_{\text{off}} = (1, 0, \ldots, 0)$ (see proposition 1 in appendix D). The existence of a stable quiescent state is expected, as the nonzero probability of synaptic failure will eventually attenuate any signal. Second, if A is well behaved in the sense that its eigenvectors have limits as $\gamma \to N$ (an assumption that is supported by numerics; see Figures 2A and 2C), then the second largest eigenvalue λ^* of A converges to 1 as $\gamma \to N$, indicating the emergence of an additional dimension of persistent activity. This too is intuitive, as a maximal connectivity strength should result in a stationary state in which all neurons fire at each layer. The catch, however, is that the corresponding eigenvector v^* converges to a vector in the subspace of bimodal or synchronous distributions—that is, to the span of v_{off} and v_{on} where $v_{\text{on}} = (0, \ldots, 0, 1)$ corresponds to all neurons firing (see proposition 2 in appendix D). All other eigenmodes must converge to 0 as $\gamma \to N$. So despite the emergence of this extra persistent dimension, activity becomes synchronous as connectivity strength increases. Ideally, what we want is

---

[2]In Markov chains with very nonnormal transition matrices, transient activity can persist past that expected solely by the spectrum; these matrices can be analyzed through their prominent pseudospectral sets, which are the eigenvalues of small perturbations of the matrix. When we pursued this type of analysis of A, we did not find significant pseudospectral sets that described the persistent activity of our networks beyond expectations from the spectral analysis (results not shown; see Trefethen & Embree, 2005, for more details on pseudospectral analysis).
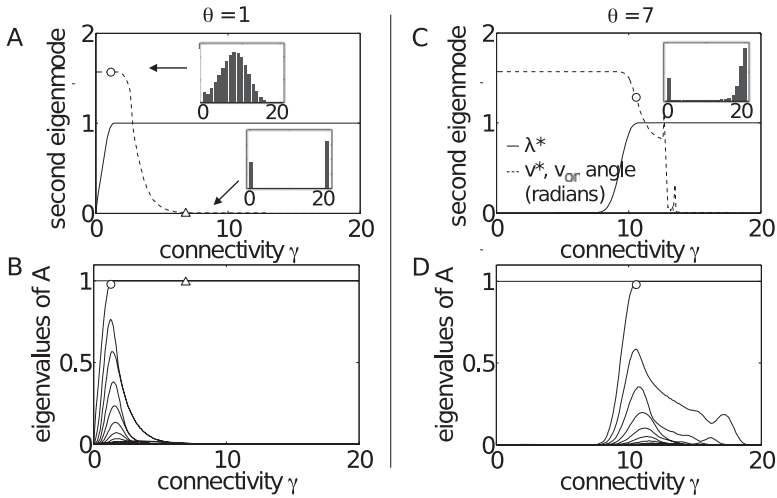
Figure 2: Spectral analysis of the mean transition matrix for networks with (A, B) $\theta = 1$ and (C, D) $\theta = 7$. (A, C) The second largest eigenvalue λ^* (solid line) effectively reaches to 1 while the angle between v^* and the vector corresponding to full synchrony v_{on} (dashed line, plotted in radians) maintains significant value for a range of γ, indicating that the second eigenmode is both persistent and far from bimodal. This is also illustrated by the insets, which show typical histograms on the line quasi-attractor either at γ_{eig} (circle markers on dashed line in panels A and C and on the second dominant eigenvalue in panels B and D) or when γ is too high to support broadly distributed eigenmodes, resulting in bimodal distributions (triangular marker in panels A and B). (B, D) Also at the emergence of the line quasi-attractor (circle markers), all eigenvalues are near maximal compared to their values over the entire connectivity range.

for λ^* to be practically 1 yet for the span of v^* and v_{off} to be far from the plane of bimodal distributions.

Intriguingly, numerical calculations reveal that this does occur for an intermediate level of connectivity γ_{eig} (see Figures 2A and 2C), implying the emergence of a plane spanned by the two principal eigenmodes v^* and v_{off} that, due to increased persistence, effectively acts as an attractor in sufficiently shallow layers: because of this, we will call this plane *quasi-attracting*. Once the vectors are normalized to represent probability distributions, this means that at γ_{eig}, there exists a line quasi-attractor that is far from the space of bimodal distributions, and hence that the network can support broadly distributed, incompletely synchronized firing states. At this same intermediate γ_{eig}, we also observe significant values of all eigenmodes (see Figures 2B and 2D), showing further persistent activity contributed by other eigenmodes, at least for the initial network layers.
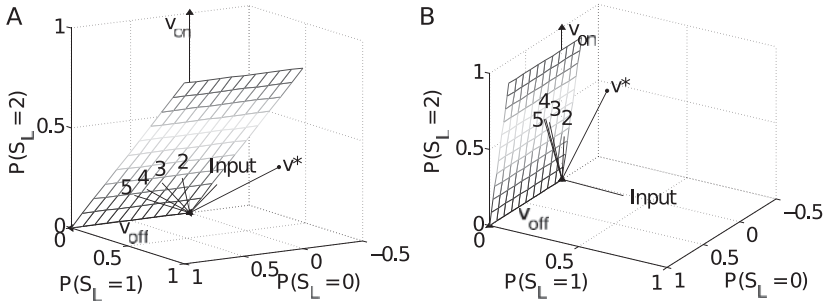
Figure 3: Geometrical interpretation of spike count propagation for $N = 2$, $\theta = 1$. The spike count histogram evolves through layers according to the mean-field model via iterated matrix multiplication, corresponding to a discrete trajectory in the space of spike count probability distributions. (A) For low connectivity strengths, the input distribution quickly converges to the plane spanned by the first two eigenmodes (the gray plane shown, although histograms will be constrained to the line embedded in the plane satisfying $\sum_i P_i = 1$) as the network encodes the signal. The distribution then slowly converges to the true stationary state v_{off}, and the signal decays. In this example, convergence to quiescence occurs in only a few layers. (B) For high connectivity levels, activity persists through the deeper layers, but the line quasi-attractor has rotated closer to the space of bimodal distributions spanned by v_{on} and v_{off}. The ideal network lies between these two figures. See the text for a more detailed discussion.

We pause to give a geometrical view of the mean-field dynamics described above. This is illustrated in Figure 3 for $N = 2$, although the following description holds for arbitrary N. Consider the $(N + 1)$-dimensional space of the spike count probability distribution at a layer. Starting with any input probability vector P_{input}, the layer-to-layer mean-field dynamics of the network can be visualized as iterated mappings of the input vector P_{input} in the space of spike count distributions, constrained to the simplex $\sum_i |P_i| = 1$. In Figure 3, repeated applications of A are enumerated. In the first couple of iterations, the spike count distribution converges toward the line quasi-attractor spanned by v_{off} and v^* as smaller eigenmodes decay. This may be interpreted as the encoding of the input distribution in the lower-dimensional quasi-attractor after a few layers. Eventually the system drifts to the stationary state where all neurons are silent, v_{off}. This of course represents a final state in which the network has "forgotten" the input. If $\gamma < \gamma_{eig}$, then the convergence to v_{off} happens within a few layers (as in Figure 3A). When $\gamma > \gamma_{eig}$, although activity persists through many layers as expected, the line quasi-attractor has rotated nearer to the span of v_{on} and v_{off}, so that the persistent activity is nearly synchronous (see Figure 3B). It

is only when $\gamma \approx \gamma_{\text{eig}}$ that activity is persistent while resisting synchrony. In this sense, γ_{eig} represents the existence of a persistent mode of activity characterized by a balance of principal eigenmodes that are broadly distributed, avoiding firing patterns being limited to synchrony or quiescence. In fact, as we explore in the following section, $\gamma \approx \gamma_{\text{eig}}$ also predicts further interesting statistical features of network responses.

5 Complexity of Network Responses

Next, we study two measures of the statistical complexity of the network responses over the range of connectivity strengths and threshold levels. First, we take an information-theoretic approach to the question of higher-order interactions, which asks: When do neurons fire in a way that cannot be predicted from their firing rates and pairwise spike correlations alone? Beyond their basic role in characterizing the degree of coordinated spiking in networks (Shlens et al., 2006; Schneidman, Berry, Segev, & Bialek, 2006; Martignon et al., 2000; Staude, Rotter, & Grün, 2010), higher-order statistical interactions have been shown to be necessary to produce broad distributions spiking activity (Amari et al., 2003; for recent applications, see Macke, Opper, & Bethge, 2011; Yu et al., 2011) and to have a significant impact on the coding of stimuli (Ganmor, Segev, & Schneidman, 2011; Montani et al., 2009).

To calculate the extent of higher-order moments in the response distributions, we use maximum entropy models (Shlens et al., 2006; Schneidman et al., 2006; Ohiorhenuan, Mechler, Purpura, Schmid, & Victor, 2010; Yu et al., 2011; Jaynes, 1957). The pairwise maximum entropy fit of a probability distribution is defined as the distribution that has maximal entropy while being constrained to match the first and second moments of the true distribution. Thus, this fit makes the fewest additional assumptions on the structure of the probability distribution; any additional structure is attributed to higher-order moments. For the permutation-symmetric networks at hand, the pairwise maximum entropy distribution takes the form of a one-dimensional discretized gaussian:

$$P^{\text{ME}}(n) = \frac{1}{Z} \exp\{\lambda_1 n + \lambda_2 n^2\}, \tag{5.1}$$

where Z is a normalizing factor and λ_1, λ_2 are the parameters chosen to match the first two moments. As a measure of the impact that higher-order correlations have in shaping the response distributions, we follow Shlens et al. (2006), Schneidman et al. (2006), Ohiorhenuan et al. (2010), and Yu et al. (2011) and compute the stimulus-averaged Jensen-Shannon (JS) divergence

between the true distribution and its maximum entropy fit:

$$D_{JS}(P_L, P_L^{ME}) = \frac{1}{2} \sum_{m=0}^{N} P_L(m) \log_2 \left(\frac{P_L(m)}{\frac{1}{2}(P_L(m) + P_L^{ME}(m))} \right)$$

$$+ \frac{1}{2} \sum_{m=0}^{N} P_L^{ME}(m) \log_2 \left(\frac{P_L^{ME}(m)}{\frac{1}{2}(P_L(m) + P_L^{ME}(m))} \right). \qquad (5.2)$$

This quantity assumes values $0 \leq D_{JS}(P_L, P_L^{ME}) \leq 1$; it can be thought of as a symmetrized version of the Kullback-Leibler divergence.

This comparison of the spike count distribution with the maximum entropy model will describe how well (over all possible networks of that particular gamma) the first two moments can describe the responses. This is a complementary view from directly calculating higher-order cumulants (Staude, Grün, & Rotter, 2010), directly quantifying how distinct the full distribution is from one with the minimal possible statistical assumptions. In the special case of fully connected layers ($C = N$), the mean-field description is exact, and hence this will correspond to the tendency of any group of $k > 2$ neurons to fire in the same bin (since the network is homogeneous). For $C < N$, this quantity approximates the amount of coincident spiking averaged over groups of k neurons.

Recall that each neuron in the first layer is independently stimulated so that their firing is a Bernoulli trial, so no correlations are injected into the network. All correlations, pairwise and higher order alike, emerge solely from the network interactions. We computed the JS divergence between spike count distributions distributions at layer 5 and their pairwise maximum entropy conditioned on input rate, then average this over all possible stimuli. Through this assessment, we note significant complexity already by the fifth layer at γ_{eig} (see Figures 4A and 4B, solid line). Beyond γ_{eig}, as firing rates approach maximal values, the JS divergence decreases to zero. This is because the JS divergence infers the effects of the higher-order moments in the response distribution beyond that which would be expected from the first two moments alone, so high firing rates alone do not necessarily imply large JS divergence (e.g., if neurons are independent with maximal firing rate, they will fire together frequently but exhibit no correlation).

How can we understand the origin of such statistical complexity? We next show that they can be predicted from the spectral analysis of the previous section, without the need for simulation. Figures 4C and 4D plot the JS divergence between the spike count histograms on the line quasi-attractor and their pairwise maximum entropy fit. Here, we plot this quantity as a function of their position along the line, parameterized so that v_{off} is at position 0. This can be compared to an average JS divergence of approximately 0.08 (dashed lines; calculated by averaging over 10,000 random sample
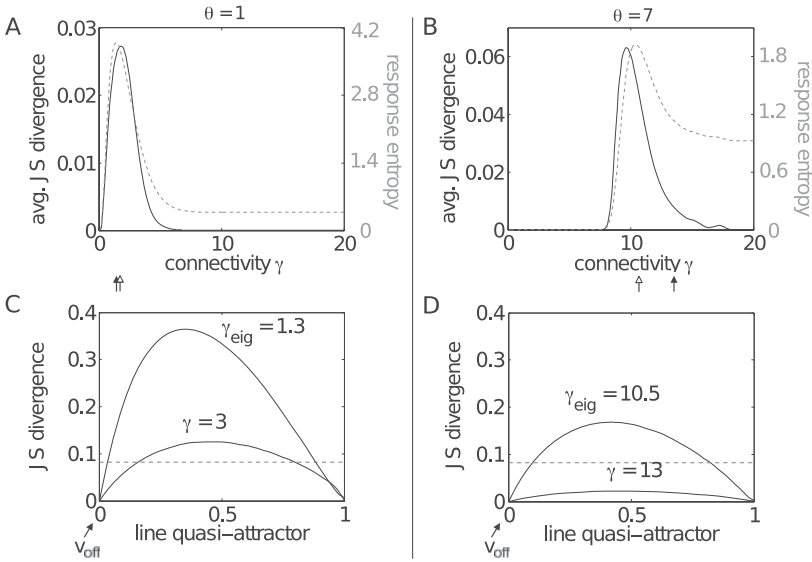
Figure 4: Statistical complexity of network responses for (A, B) $\theta = 1$ and (C, D) $\theta = 7$. (A, C) Response entropy (dashed gray line) and the stimulus-averaged JS divergence between the true distribution at layer 5 and the pairwise maximum entropy fit (solid black line) plotted as a function of γ. Also shown are γ_{eig} (hollow arrow below panel) and γ_{obs} (solid arrow). (A) When $\theta = 1$, peaks in both curves line up with γ_{eig}, as does γ_{obs} (arrows offset for visibility). (B) For higher-threshold networks, γ_{obs} does not align with γ_{eig} or other assays (see section 6). (C, D) JS divergence between spike count histograms and their maximum entropy fits along the line quasi-attractor (solid lines; axis parameterizes distributions along the line quasi-attractor starting at v_{off}). Compare with the divergence averaged over the entire space of histograms (dashed lines).

distributions so that the mean had converged) over the entire space of possible response histograms. In particular, the eigenvectors at γ_{eig} produce significantly larger statistical complexity than the average. This is because at this level of connectivity, the response distribution is a mixture of two distributions: a large component of quiescent neurons corresponding to v_{off} and a broader component corresponding to the contribution of v^*. As θ increases, the level of the JS divergence decreases on the line quasi-attractor as higher thresholds reduce the breadth of v^*.

The second statistical feature of note is the response entropy of the spike count distribution:

$$H(P(S_L)) = \sum_{n=0}^{N} P(S_L = n) \log_2 P(S_L = n). \tag{5.3}$$

Larger response entropies indicate broader response distributions. The response entropy at the fifth layer peaks at γ_{eig}, indicating that the emergence of the line quasi-attractor corresponds to the broadest distribution of activity across all values of γ (see Figure 4, dashed gray line). However, the peak response entropy decreases for higher values of θ; this is the result of the fact that as θ increases, v^* produces less broad response distributions due to the high threshold and hence the silencing of weak inputs, preventing them from eliciting any firing in the subsequent layer.

In sum, we have shown that at γ_{eig}, networks display an emergence of statistical complexity—through both maximal response entropy and significant contributions from higher-order moments within responses—directly because of the contribution of other eigenmodes at that level of connectivity.

6 Combining Neutral Stability and Broad Response Distributions

In order to maintain averaged levels of activity without succumbing to synchrony, a network must simultaneously satisfy two criteria. First, it must be able to preserve averaged firing rates from layer to layer without succumbing to either runaway excitation and maximal firing rates in deeper layers or to decaying network activity. Second, a network must exhibit a broad spike count distribution at each layer in order to prevent the buildup of correlations and synchrony (Kumar et al., 2010; Reyes, 2003; Litvak et al., 2003). We refer to these properties, taken together, as asynchronous rate coding.

For which parameter regimes can such asynchronous rate coding occur? To quantify this, we need an assay that captures how well networks are able to propagate broad response distributions from one layer to the next. We base this on the propagation of binomial spike count distributions, as these correspond to fully independent activity in each layer. Specifically, we define the spike count JS divergence D to be the JS divergence (see equation 5.2) between the binomial input distribution P_1 and the Lth layer spike count distribution P_L averaged over all stimuli S:

$$D(\gamma, \theta) = \frac{1}{N+1} \sum_{n=0}^{N} D_{JS}(P(S_L|S=n), P(S_1|S=n). \tag{6.1}$$

Networks will exhibit good performance, measured by low values D, when they maintain the broad (independent) spike count distribution and the averaged firing rate that occurs in the first layer.

Plots of the spike count JS divergence over γ are shown in Figure 5 for increasing values of the spike threshold θ. For each fixed θ, there is an optimal, intermediate value of γ at which networks are best able to satisfy both of our criteria. However, as the threshold level increases, the best value
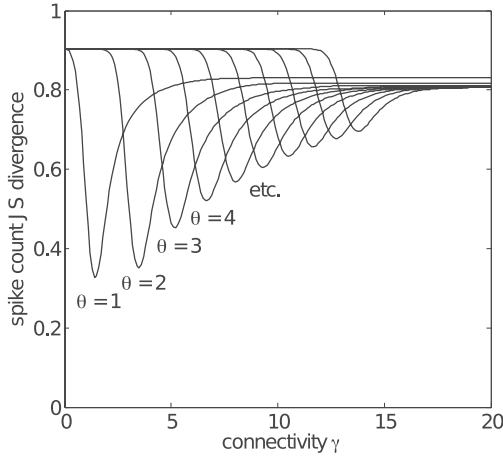
Figure 5: Spike count JS divergence plotted as a function of γ for increasing θ. Optimal performance for each threshold (the minimum value of the curve) occurs near γ_{eig}.

of the spike count JS divergence also increases, showing that high-threshold networks fail to produce asynchronous rate coding.

This failure follows from the requirements of neutral dynamics and broad response distributions described in previous sections. First, from section 3, γ_{obs} captures the first criterion of complex signal coding outlined above; that is, networks demonstrate neutral stability and average one-to-one rate transmission when they average a branching ratio of $\sigma \approx 1$. On the other hand, section 4 shows that γ_{eig} reflects when the network supports persistent, broad response distributions, providing an assay of the second criterion. Complex signal propagation can therefore occur in these systems only when $\gamma_{obs} \approx \gamma_{eig}$. Comparing Figure 2 with the previous Monte Carlo simulations in Figures 1B and 1C reveals that both criteria can be simultaneously satisfied when few inputs are required to cause a spike, but a gap between these required values of connectivity γ appears with increasing θ. To be precise, for $N = 20$, $\theta = 1$, Monte Carlo simulations and spectral analysis both yield $\gamma_{obs} \approx \gamma_{eig} \approx 1.3$. When $\theta = 7$, however, simulations show $\gamma_{obs} \approx 13.75$ yet $\gamma_{eig} \approx 10.5$. As shown through the eigenstructure, at γ_{obs}, only bimodal activity is supported after a few layers in high-thresholding networks. In fact, because of the inevitable synchrony in deep layers, optimal performance under the JS divergence tends to fall nearer to γ_{eig} than to γ_{obs}. Networks of high-threshold neurons are therefore unable to simultaneously satisfy both requirements of complex signal propagation outlined at the beginning of this section.

Intuitively, the reason that $\gamma_{\text{obs}} > \gamma_{\text{eig}}$ is that networks with high-threshold neurons reject inputs of low firing rate, so that when θ is large, there is an increased likelihood that connectivity structure and stochasticity will conspire to silence all activity in the next layer. Geometrically speaking, as θ increases, so does the nullity of A, resulting in a larger and larger subspace that trajectories must avoid lest they risk susceptibility to network quiescence; in order to reach an average of one-to-one rate transmission, it is necessary to provide a buffer for the coding subspace from the null-space by inflating the connectivity into the regime of bimodality.

Also of practical importance is the question of robustness to parameters. The delicate nature of γ_{eig} and γ_{obs} constrains networks that produce asynchronous rate coding to finely tuned connectivity strengths; one requires that the branching ratio lie at a critical value $\sigma \approx 1$, while the other relies on a precise balance between persistent yet broadly supported eigenmodes. This sensitivity is reflected in the sharp troughs in the JS divergence (see Figure 5); for even larger N, these troughs become even sharper, and robustness is a more important goal to obtain. As we will see in the next section, however, this sensitivity can be mitigated by adding an inhibitory population to each layer.

To summarize results thus far, we evaluate networks on two criteria: $\sigma \approx 1$ and broad response distributions. Low-threshold networks can always satisfy broad response distributions and maintain average rate transmission at the same γ. High-threshold networks are able to somewhat support broad distributions, although the preserved aspects of network responses and their lower values of response entropy indicate less broad distributions as compared to their low-threshold counterparts. They also can satisfy $\sigma \approx 1$; however, this is due to averaging: because of the increasing nullity of the mean transition matrix, these networks cannot propagate weak input stimuli, so they must overcompensate by inflating γ. Because of this, no high-threshold network of a fixed γ can simultaneously satisfy both criteria, and hence they cannot propagate rates asynchronously through layers. This appears to be a significant limitation for high-threshold networks—and, importantly, for many biological neural networks in which many inputs are required to elicit a spike. In the following sections, we incorporate additional biophysical features, inhibition and noise, and study whether this provides a resolution so that high-threshold networks can support persistent, broadly distributed activity.

7 Excitatory-Inhibitory Networks Display Increased Robustness

How can asynchronous rate propagation emerge in high-threshold networks? Intuitively, we might expect an added inhibitory population to prevent runaway excitation and saturation of firing rates to high values, thus preventing synchrony. To test this, we added an inhibitory population

of N_I neurons to each layer of $N_E = N - N_I$ excitatory neurons and further impose $N_E - N_I > \theta$ (otherwise no activity could be transmitted due to the homogeneity in network connectivity—even if only the excitatory population is active in layer L, the random connectivity imposed will cause the same proportion of the excitatory and inhibitory populations in layer $L + 1$ to fire). Network parameters are assumed to be homogeneous among the inhibitory and excitatory populations. Because of this assumption, it is straightforward to calculate the new four-dimensional mean-field transition matrix A_{in}:

$$P\big(S_L^E = m_E, S_L^I = m_I | S_{l-1}^E = n_E, S_{l-1}^I = n_I\big)$$

$$= \binom{N_E}{m_E} q_{n_E,n_I}^{m_E} (1 - q_{n_E,n_I})^{N_E - m_E} \times \binom{N_I}{m_I} q_{n_E,n_I}^{m_I} (1 - q_{n_E,n_I})^{N_I - m_I}, \quad (7.1)$$

where S_L^i is the number of cells spiking in the excitatory ($i = E$) or inhibitory ($i = I$) population at the Lth layer and q_{n_E,n_I} is the probability that a downstream neuron spikes given n_E spiking excitatory neurons and n_I spiking inhibitory neurons in the upstream layer:

$$q_{n_E,n_I} = \sum_{k_E=\theta}^{n_E} \sum_{k_I=0}^{\min(n_I, k_E - \theta)} \binom{n_E}{k_E} \left(\frac{\gamma}{N}\right)^{k_E} \left(1 - \frac{\gamma}{N}\right)^{n_E - k_E}$$

$$\times \binom{n_I}{k_I} \left(\frac{\gamma}{N}\right)^{k_I} \left(1 - \frac{\gamma}{N}\right)^{n_I - k_I}. \quad (7.2)$$

The binomial input distributions now take the following form:

$$P(S_1^E = m_E, S_1^I = m_I | S = n)$$

$$= \binom{N_E}{m_E} \left(\frac{n}{N}\right)^{m_E} \left(1 - \frac{n}{N}\right)^{N_E - m_E} \times \binom{N_I}{m_I} \left(\frac{n}{N}\right)^{m_I} \left(1 - \frac{n}{N}\right)^{N_I - m_I}. \quad (7.3)$$

The expression for the transition matrix for the excitatory-inhibitory networks has a similar form to that of the purely excitatory networks, so the eigenstructure of A_{in} (see equation 7.1) is similar to that of A (see equation 4.1): it has a unique stationary state corresponding to all neurons being quiescent, and as $\gamma \to N$, the second largest eigenvalue converges to 1 and its eigenvector corresponds to bimodality (see proposition 3 in appendix D). There also is an intermediate state of connectivity at which $\lambda^* \approx 1$ and v^* is far from bimodal (see Figures 6A and 6B). Here we consider
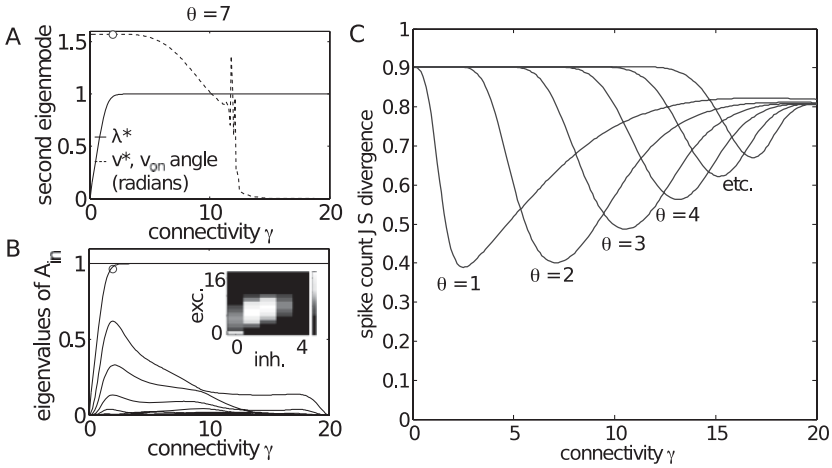
Figure 6: Excitatory-inhibitory networks display increased robustness, $N_E = 16$ and $N_I = 4$. (A) The second largest eigenvalue λ^* and the angle between v^* and v_{on} (dashed line) overlap over a larger parameter space, indicating robustness at γ_{eig}. (B) Similarly, all eigenvalues A have broader peaks. The inset shows a typical broadly distributed histogram at γ_{eig} (indicated by the marker in panels A and B). (C) The spike count JS divergence has a wider minimum for all values of θ, showing that inhbition also allows more robust asynchronous rate propagation.

$\theta = 7$, as well as $N_E = 16$, $N_I = 4$ to simulate about 20% inhibition, as typically used in, for example, cortical modeling (Braitenberg & Schüz, 1998).[3] This yields $\gamma_{eig} \approx 16.9$. However, according to Monte Carlo simulations, the branching ratio is always less than 1 for all $\gamma < N$. Firing rates thus fail to be maintained in this network, as reflected in the spike count JS divergence in Figure 6C. The reason is that A_{in} is structurally similar to A: as in the purely excitatory networks, the high threshold still rejects weak inputs and sends them to the stationary state of quiescence, v_{off}. This is in agreement with Reyes (2003), who found that adding a homogeneous inhibitory population to each layer does not help networks avoid synchrony.

Inhibition does, however, increase the robustness of JS divergence to perturbations in connectivity strength γ. Specifically, the troughs of minimal

---

[3]We emphasize that the results in this section are not particular to these specific choices of N_I and N_E. As long as $N_E - N_I > \theta$, the intermediate γ_{eig} producing broad, persistent distributions will continue to exist. Other results regarding robustness and limitations on asynchronous rate propagation for high θ also continue to hold.

JS divergence widen compared to those of purely excitatory networks (see Figure 6C). This is reflected as well in the eigenstructure: the intermediate state of persistent, broadly distributed distributions is now stretched to cover a wider range of γ (see Figures 6A and 6B). This robustness grows as the size of the inhibitory population is increased so long as $N_E - N_I > \theta$ (results not shown). Intuition for this effect can be obtained by comparing to the purely excitatory case for large N. On average, each neuron in this case has synaptic input of size γ. To produce a broad range of responses and avoid either too many inputs (resulting in maximal firing rates) or too few (resulting in quiescence), γ must hover near some critical value that depends on parameters. Now suppose we add a population of N_I inhibitory neurons: then each neuron has on average $1/N(N_E - N_I)\gamma$ net synaptic input. Since $N_E - N_I < N$, this slope is shallower than that for purely excitatory networks, so the networks are more robust to chance perturbations around the critical value of inputs, and hence to connectivity strength. Simulations agree with this scaling argument (see appendix E, especially Figure 11).

Increased robustness to connectivity parameters in the presence of inhibition is interesting as it addresses a major concern regarding the plausibility of dynamics at critical transition values of connectivity (as discussed in the previous section). In sum, inhibition may help resolve the need for fine-tuning by enhancing robustness to fluctuations in network connectivity.

8 Impact of Background Noise

The next attempt to recover asynchronous rate propagation follows from van Rossum et al. (2002), in which a noisy background current was shown to enhance the preservation of firing rates in feedforward networks of integrate-and-fire neurons (see also Nowotny & Huerta, 2003; Reyes, 2003; Litvak et al., 2003). We inject background noise in the form of independent, zero-mean gaussian independent noise current χ to each neuron, $\chi \sim \mathcal{N}(0, \sigma_\chi^2)$. This transforms the Heaviside-like thresholding into a smoother, sigmoidal operation. The probability that a neuron will spike given n cells firing in the upstream layer is now

$$q_n = \int_{-\infty}^{\infty} Pr(I > \theta - x)Pr(\chi = x)\,dx,$$

where I is the synaptic input from the upstream layer without the additional noise component. If $x > \theta$, then the neuron fires with probability 1 because the noise alone is enough to elicit a spike. If $x < \theta - n$, the neuron can never fire, as even the addition of all upstream neurons delivering input would
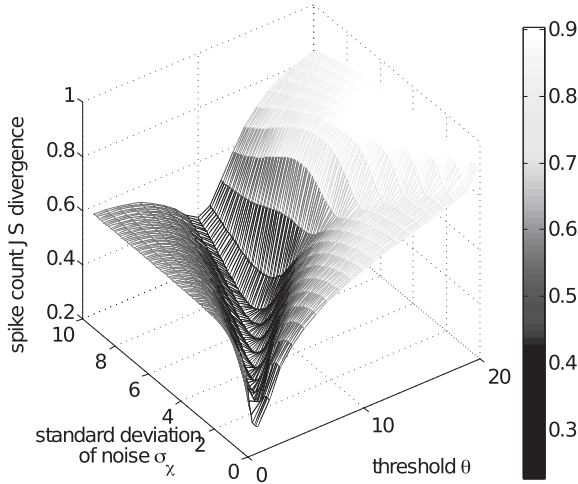
Figure 7: Impact of noise on input propagation. Surface shows spike count JS divergence as a function of θ and the standard deviation of noise added to each neuron, σ_χ. For each θ, there is a σ_χ that optimizes asynchronous rate propagation. For $\theta < 10$, the relationship between θ and optimal σ_χ is linear.

be insufficient to cross threshold. We can then rewrite q_n as

$$q_n = \int_{\theta-n}^{\theta} \frac{1}{\sqrt{2\pi}\sigma_\chi} \exp\left(-\frac{x^2}{2\sigma_\chi^2}\right) \left[\sum_{k=\lceil\theta-x\rceil}^{n} \binom{n}{k}\left(\frac{\gamma}{N}\right)^k \left(1-\frac{\gamma}{N}\right)^{n-k} \right] dx$$

$$+ \int_{\theta}^{\infty} \frac{1}{\sqrt{2\pi}\sigma_\chi} \exp\left(-\frac{x^2}{2\sigma_\chi^2}\right) dx. \tag{8.1}$$

Nowotny and Huerta (2003) consider a similar expression (equation 7 in their paper), although both the exact form of their expression, and their conclusion that it has little effect on the transition matrix, differ from ours. We denote by A_{noisy} the transition matrix describing these networks with added noise, generated by the new q_n.

Figure 7 plots the spike count JS divergence (see equation 6.1) as a function of θ and σ_χ. The main result is that adding the right amount of noise produces lower values of JS divergence—and thus more consistent propagation of asynchronous inputs—at larger values of θ. This result agrees with the findings of van Rossum et al. (2002) (cf. their Figure 2B and see appendix F for further comparisons with this study). Our result is also in agreement with Reyes (2003), who finds that adding white noise as a background current reduces the amount of synchrony present in networks.

For each of the threshold values θ shown, there is an optimal σ_χ for asynchronous rate propagation (i.e., that minimizes the JS divergence). This amount of noise gives spontaneous firing rates of less than 12%, as measured by the probability $Pr(\chi > \theta)$. For the remainder of this section, we will take the optimal value of noise for each value of threshold. Figure 8C uses these values to provide another view of optimized JS divergence, which reveals the improvement in comparison with noise-free networks (see Figure 5). Moreover, γ_{obs} and γ_{eig} do coincide in the noisy case, even for high values of θ (at about 14.25 in for $\theta = 7$, branching ratio figure not shown).

One might expect the optimal level of noise to decrease for networks with more layers. Counter to this intuition, however, we find that the optimal noise level does not depend strongly on the number of layers.[4] This is because the optimal noise levels have the effect of eliciting at each layer the amount of spontaneous background firing that will precisely balance the probability that the signal will terminate due to synaptic failure or chance redundant (i.e., highly convergent) connections. Therefore, optimal noise levels reduce an inherent asymmetry of the model that allows transitions from high firing rates to quiescence, but not the other way around.

In contrast to the effects of inhibition, the addition of background noise does produce substantial changes in the structure of the transition matrix. For example, comparing A_{noisy} with A, spontaneous activity is now possible, as v_{off} is no longer the stationary state. Instead, the stationary state v_{SS} is now a function of γ. In particular, the noise contributes a nonzero probability from transitioning from any state to any other state, so the components of A_{noisy} are strictly positive. By the Perron-Frobenius theorem, this means the system has a unique stationary state v_{SS} whose components are all strictly positive (so it can never be v_{on} or v_{off}). Computationally we find that the second largest eigenvalue now does not converge to 1 as $\gamma \to N$; it does, however, attain a peak value near 1 at an intermediate γ_{eig}, and at this point v_{SS} and v_{off} are also far from bimodal (see Figures 8A and 8B). Thus despite the differences in eigenstructure between A and A_{noisy}, the predominant features that define the existence of a persistent set of broad firing distributions are still apparent: there is an intermediate connectivity level γ_{eig} at which all eigenvalues are significant, the second largest eigenvalue in particular is close to 1, and both the stationary distribution and the second eigenmode are far from bimodal.

Finally, to put the role of noise to a more demanding test, we test its impact on the capacity of networks to discriminate among different input stimuli. For this, we calculate the rate discriminability by measuring the error rate given by the maximum likelihood estimator on T trials. Specifically,

---

[4]For these parameters, we find an optimal noise level of $\sigma_\chi = 0.3$ for 5 layers and $\sigma_\chi = 0.4$ for 20 layers (for $\theta = 1$). For the high-threshold case of $\theta = 7$, we find that the optimal $\sigma_\chi = 4.6$ for both 5- and 20-layer networks.
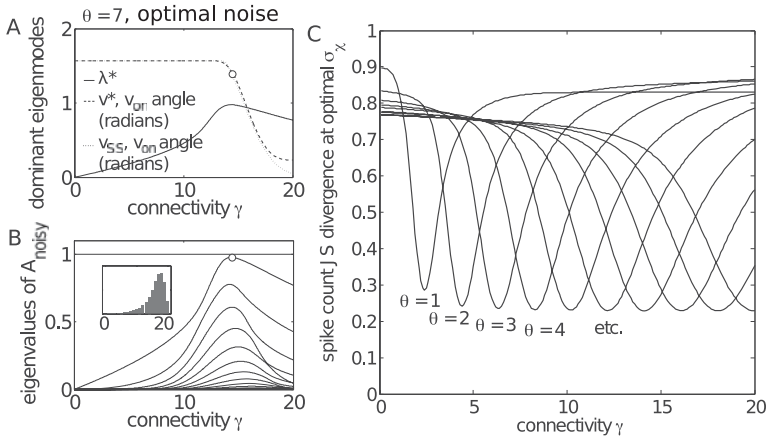
Figure 8: Properties of noisy networks at optimal background noise levels. (A) The second largest eigenvalue λ^* peaks very close to 1 at an intermediate γ_{eig}. The angles between v^* and v_{on} (dashed line, plotted in radians) and between v_{SS} and v_{on} (dotted line, plotted in radians) have large values at γ_{eig}. (B) At this same value γ_{eig}, all eigenmodes have a significant contribution. The inset shows a typical broadly distributed histogram at γ_{eig} (indicated by the marker in panels A and B). (C) The spike count JS divergence, taking the optimal value of σ_χ for each θ. With optimal noise values added, asynchronous rate propagation is dramatically improved for high-threshold networks.

suppose the network produces output spike counts $S_L^1, \ldots, S_L^T$ under some fixed input stimulus level S. Since the trials are independent, the maximum likelihood estimator (MLE) chooses between two stimuli S and S' by selecting the one that is more likely to result in the given data, via the likelihood ratio:

$$\prod_{j=1}^{T} \frac{P(S_L^j|S)}{P(S_L^j|S')}.$$

If this product is greater than 1, the MLE chooses stimulus S; less than 1, and the MLE chooses stimulus S'. Assuming S and S' are equally likely a priori, the error rate is given by

$$\text{ER}(S, S') = \frac{1}{2}\mathbb{E}\left[\mathbb{I}\left(\prod_{j=1}^{T} \frac{P(S_L^j|S)}{P(S_L^j|S')} > 1\right)\Big|S'\right]$$

$$+ \frac{1}{2}\mathbb{E}\left[\mathbb{I}\left(\prod_{j=1}^{T} \frac{P(S_L^j|S)}{P(S_L^j|S')} > 1\right)\Big|S\right], \tag{8.2}$$
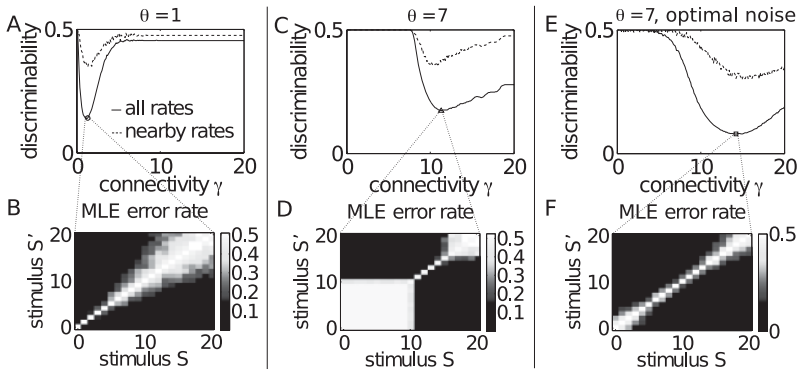
Figure 9: Rate discriminability for noise-free networks with (A, B) $\theta = 1$ and (C, D) $\theta = 7$, as well as (E, F) a network with $\theta = 7$ and optimal noise, $\sigma_\chi = 4.2$. (A, C, E) Nearby discriminability (dashed line) and average discriminability (solid line) for $T = 25$ trials plotted as a function of connectivity level γ. (A) For low-threshold networks, rate discriminability is optimal at γ_{eig}. (C) For high-threshold networks, nearby discriminability is best near γ_{eig}, but this minimum is shifted for average discriminability. (E) Adding noise improves rate discrimination in high-threshold networks. (B, D, F) Maximum likelihood error rate plotted for every possible pair of input stimuli before averaging. The chosen networks are those that minimize average discriminability, as indicated by the markers in panels A, C, and E.

where the first expectation is taken over the distribution $P(\cdot|S')$ and the second over $P(\cdot|S)$. This produces an $(N+1) \times (N+1)$ matrix describing the MLE error rate for distinguishing S from S'. We then average over either the entries in the entire matrix to give the average discriminability, or we average the entries in the superdiagonal to give the nearby discriminability, that is, the discriminability between nearby rates.

Figures 9A and 9C first summarize discriminability in the absence of noise. Rate discriminability reaches its minimal value at $\gamma_{\text{eig}} \approx \gamma_{\text{obs}}$ when $\theta = 1$; when $\theta = 7$, the minimal discriminability does not exactly coincide with either γ_{eig} or γ_{obs}. A glance at the MLE error rates without averaging reveals the particular type of computation performed in each case: Figures 9B and 9D show the error rates at the values of γ that yield the lowest average discriminability, as indicated by the markers in Figures 9A and 9C. Low-threshold networks are able to accurately discriminate between rates over the entire stimulus space, including nearby rates. High-threshold networks, although able to perfectly distinguish a few rates in a limited intermediate range, cannot at all distinguish between nearby high rates or low rates. Rather, these networks are better suited to classifying input rates into two bins: low and high.

Interestingly, the added background noise promotes better discriminability between rates in high-threshold networks, dropping the minimal level to values even below that of noise-free, low-threshold networks (see Figure 9E). Moreover, the MLE error rates (see Figure 9F) show a marked improvement in the ability to distinguish between nearby rates at γ_{eig}, as revealed by the tightly banded matrix structure. Not only does noise improve rate propagation in neurons, it also changes the computation from a coarsely grained classifier to one with more resolution. This is a specific example of the more general phenomenon of stochastic resonance (see, e.g., McDonnell & Abbott, 2009; Longtin, 1993).

9 Discussion

9.1 Summary. In this letter, we study the transitions in feedforward network dynamics that occur as connectivity strength and firing threshold are varied. We characterize these transitions via critical branching, neutral stability, higher-order correlations, and broad firing distributions. After quantifying critical branching by computing the branching ratio, we show that neutral stability (persistence of firing patterns from one network layer to the next), together with statistical properties of the persistent patterns, can be predicted via a spectral analysis of the underlying mean-field transition matrix. Throughout most of the parameter space, persistent activity is restricted to highly bimodal, synchronous responses, as found by Reyes (2003), Nowotny and Huerta (2003), and Litvak et al. (2003). However, there are transition connectivity levels that yield persistent, broadly distributed spike count histograms with higher-order correlations and large response entropy. For low-threshold networks, this occurs simultaneously with (approximately) critical branching, revealing that such networks are well suited to transmitting rates without synchronization. On the other hand, high-threshold networks do not produce both critical branching and broad response distributions at the same connectivity strength; when the former is satisfied, these networks tend to produce synchronous responses.

Interestingly, adding further biologically motivated features increased the robustness of transitions in high-threshold networks. In particular, simulations and spectral analysis show that including an inhibitory cell population extended the connectivity range that yields asynchronous propagation of inputs. Adding zero-mean noise to each neuron had a similar effect and also improved the discriminability of inputs, echoing the findings of van Rossum et al. (2002) in integrate-and-fire networks.

We conclude that networks with low firing thresholds, or those in which intrinsic noise elevates firing probabilities, exhibit a set of dynamical and statistical signatures associated with critical transitions in network activity.

9.2 Connections with the Criticality Literature. We now discuss links with the broader literature on criticality, which suggests that the brain may operate at a state characterized by complex dynamics, significant higher-order correlations, and enhanced computational properties. This is often described as operating on the boundary between ordered and irregular (or chaotic) activity. In particular, such systems can flexibly perform a wide range of operations on time-dependent inputs when their recurrent networks lie near the critical state, which is defined by calculating the expected neutral separation of trajectories using a mean-field model (Bertschinger & Natschlager, 2004; Legenstein & Maass, 2007).

Along these lines Beggs and Plenz (2003) motivate a feedforward model based on array recordings.[5] Here, the authors compute the mutual information between the 2^N possible binary "words" at the first and last layers. Intriguingly, they numerically show, for the low-threshold case $\theta = 1$, that the mutual information is maximized for the same parameters at which critical branching occurs. Our finding in the averaged, mean-field setting echoes this result. An interesting extension of our work would be to explain the findings of Beggs and Plenz (2003) using the spectral properties of the allied layer-to-layer transition matrix between binary words. In principle, such an approach could predict the occurrence of cascades of such words over multiple network layers and their role in encoding stimuli.[6]

9.3 Verifying and Extending the Model. We imposed a number of simplifications in this letter to achieve analytical tractability. The most prominent of these is that our neurons are modeled as simple thresholding units with no intrinsic properties or time dependence (Nowotny & Huerta, 2003). An important extension is to consider how results might change if neurons included a finite integration time. For example, in excitatory-inhibitory networks, timing of inhibitory spikes will effect action potential generation (Gabernet, Jadhav, Feldman, Carandini, & Scanziani, 2005). While this can increase the selectivity of synfire chain propagation (Kremkow, Perrinet, Masson, & Aertsen, 2010), the effect on rate transmission is unknown. More generally, if both an integration timescale and a refractory period are included, the collapsing of C and p into a single parameter, a key to our mean-field approach, may not be accurate in certain cases. Specifically, this could occur when C is high and p is low, as interaction

---

[5]The authors argue that a feedforward model is appropriate in this context as electrode sites are rarely active more than once during the cascades of neural activity that they study.

[6]Such cascades are called neuronal avalanches and have been the focus of a number of experimental and theoretical studies (Beggs & Plenz, 2003; Kitzbichler, Smith, Christensen, & Bullmore, 2009; Hahn et al., 2010; Petermann et al., 2009; Hennig, Adams, Willshaw, & Sernagor, 2009; Mora & Bialek, 2011).

between different waves of propagation through the chain will allow for synaptic facilitation, whereas the opposite relationship (low C and high p) will allow combinations of synaptic facilitation with refractory periods. It is hard to say for certain how these details will affect our results without direct simulation or analysis. However, our results agree with those in networks of more realistic neurons (van Rossum et al., 2002; Reyes, 2003; Rosenbaum et al., 2010; Kumar et al., 2010). We therefore believe that our findings give a reasonable description of rate propagation in feedforward networks and provide a good intuition for these systems in a tractable manner.

Another possible limitation is that the numerical studies presented above use a fixed value of $N = 20$ neurons. However, our analytical results on spectral properties of the transition operator are independent of this choice. Moreover, we verified that our main qualitative results are preserved, for example, for the larger value $N = 100$ (taking $\theta = 1, 5, 10, 20, 35$; data not shown). In more detail, as with the smaller network, the system at $N = 100$ remains well described by a mean-field transition matrix (in fact, due to the larger population size, it is an even better fit). The eigenstructure of these matrices reveals an intermediate γ_{eig} at which the second dominant eigenmode is both persistent and broadly distributed, and there is significant contribution from all eigenvalues as well as maximal response entropy. For $\theta = 1$, this value overlaps with γ_{obs}, but as the threshold increases, the gap between the two widens; accordingly, the spike count JS divergence increases. As for the $N = 20$ case, while inhibition does continue to increase this range, the optimal performance is not improved. The addition of noise in large networks, however, has similar beneficial effects: an optimal amount of noise lowers the minimum JS divergence to around 0.32 for high values of θ. This amount of background noise required generates less than 10% probability of spontaneous firing, similar to that obtained at $N = 20$. However, one difference at $N = 100$ is that the optimal performance under the JS divergence metric D is lower: when $\theta = 1$, the optimal network attains at best a score of 0.58, compared to 0.33 for $N = 20$. Moreover, in the larger network the "well" in D values near the optimal γ value is even narrower, requiring a finer tuning of γ. These findings suggest that while our findings remain qualitatively similar for larger networks, there may be interesting new phenomena in the continuum limit of large N, an interesting subject for future study.

On another note, we focused on only a few of the many metrics of signal propagation and coding that could be applied to the networks at hand. We note further results on one of these in the appendix F, which van Rossum et al. (2002) used to measure propagation of firing rates via trial-to-trial variance of responses in deep layers. This showed similar results to our measure D of JS divergence between input and output distributions over intermediate firing rates; the two measures showed distinctions at extreme

firing rates, assessing the quiescent or saturating patterns that occur there differently (see appendix F).

We close by noting experimental predictions of our work, as could be tested directly in in vitro feedforward networks (using the techniques of Reyes, 2003) or, with the considerations above, could predict dynamics in recurrent systems as well. First, asynchronous rate propagation should become possible when the membrane potentials of neurons are biased upward (equivalent to decreasing the spike-generation threshold). Second, this also occur when sufficient noise is added local to each cell (some white noise has already been shown to reduce synchrony in Reyes, 2003), and the optimal amount of white background noise should be independent of the number of layers. Finally, adding an inhibitory population at each layer should increase the robustness of asynchronous propagation to network connectivity and synaptic strength.

Appendix A: Important Symbols and Their Descriptions

N	Number of neurons per layer
L	Number of layers
θ	Threshold level
C	Number of downstream neurons connected to each neuron in the previous layer
p	Probability of synaptic transmission
S	Input spike count
γ	Connectivity strength $\gamma = Cp$
$\mathbf{x}_L$	Activity pattern in layer L (2^N possible values)
E_L	Connectivity matrix between layers L and $L+1$
$\hat{E}_L$	Effective connectivity matrix (including instantiations of p)
E	$N \times N \times L$ connectivity tensor of the entire network
σ	Branching ratio averaged over E, p, $\mathbf{x}_1$, and S
S_L	Spike count at layer L
γ_{obs}	Connectivity strength at which $\sigma \approx 1$ is observed via simulation
A	$(N+1) \times (N+1)$ mean-field transition matrix
q_m	Probability that a neuron will fire given n spiking neurons in the previous layer
P_L	$(N+1)$-vector whose elements are the probabilities that $S_L = 0, \ldots, N$
λ^*	Second largest eigenvalue of A
v_{off}	Stationary state and dominant eigenmode of A, corresponding to quiescence
v_{on}	Histogram of all neurons firing (not an eigenvector except for $\gamma = N$)
v^*	Second dominant eigenmode of A (not a probability distribution)
γ_{eig}	Connectivity strength at which $\lambda^* \approx 1$ yet v^* is far from bimodal

P_L^{ME}	Pairwise maximum entropy fit of P_L
D_{JS}	Jensen-Shannon divergence
D	Spike-count JS divergence, $D_{JS}(P_L, P_1)$ averaged over stimuli
N_E	Number of excitatory neurons per layer
N_I	Number of inhibitory neurons per layer
A_{in}	Mean-field transition matrix for excitatory-inhibitory networks
σ_χ	Standard deviation of background noise
A_{noisy}	Mean-field transition matrix for excitatory networks with background noise
v_{SS}	Nonquiescent stationary state, dominant eigenmode of A_{noisy}

Appendix B: Derivation of Mean-Field Markov Chain

In this appendix, we outline how to obtain a formula for the mean-field Markov chain starting from the stochastic equations. The derivation is pedagogic in nature; that is, it is intended to describe in principle the assumptions inherent in the mean-field model rather than provide a practical method of calculation of equations 4.1 and 4.2. The transition probabilities are found through combinatorial arguments and were originally studied in Nowotny and Huerta (2003).

As stated in the text, the main assumption here is that neurons within a layer are permutation symmetric. This appendix describes how to obtain the mean-field Markov chain on spike counts (averaged over all connectivity architectures of connectivity strength γ) from the exact Markov chain on spiking patterns given a particular connectivity architecture E. The first step is to determine the probability that given true connectivity matrix E_L, the instantiated "effective" connectivity matrix is $\hat{E}_L$:

$$P(\hat{E}_L|E_L) = p^{K(\hat{E}_L)}(1-p)^{K(E_L - \hat{E}_L)},$$

where $K(M)$ is the number of nonzero elements in matrix M. Each element of the transition matrix in pattern space is then given by

$$P(\mathbf{x}_L = x|\mathbf{x}_{L-1} = \tilde{x}, E_L) = \sum_{\hat{E}_L} P(\hat{E}_L|E_L) \cdot \delta\big(x - \Theta(\hat{E}_L \tilde{x} - \theta)\big),$$

where δ denotes the Kronecker delta. In two steps, we will reduce the dimension of the system to condense pattern space into rate space. First, summing over x,

$$P(S_L = m|\mathbf{x}_{L-1} = \tilde{x}, E_L) = \sum_x P(\mathbf{x}_L = x|\mathbf{x}_{L-1} = \tilde{x}, E_L) \cdot \delta\left(m - \sum_{i=1}^N x(i)\right).$$

Another sum gives the $(N + 1) \times (N + 1)$ transition matrix conditioned on the connectivity matrix E_L:

$$P(S_L = m|S_{L-1} = n, E_L) = \sum_{\tilde{x}} P(S_L = m|\mathbf{x}_{L-1} = \tilde{x}, S_{L-1}, E_L)$$

$$\cdot P(\mathbf{x}_{L-1} = \tilde{x}|S_{L-1}, E_L)$$

$$= \sum_{\tilde{x}} P(S_L = m|\mathbf{x}_{L-1} = \tilde{x}, E_L) \cdot P(\mathbf{x}_{L-1} = \tilde{x}|S_{L-1}).$$

Finally, averaging over every possible E_L for the fixed γ, we obtain the elements of the mean field transition matrix,

$$A_{nm} = P(S_L = m|S_{L-1} = n)$$

$$= \sum_{E_L} P(S_L = m|S_{L-1} = n, E_L) \cdot P(E_L),$$

which gives the elements of the mean-field transition matrix. Through these steps, the explicit derivation of the mean-field model (see equations 4.1 and 4.2) from the original setup is demonstrated.

Finally, we can calculate the specific values of A_{nm} in equation 4.1 as follows. Suppose m neurons are firing in the upstream layer. Assuming conditional independence of neurons within a layer, the probability of pattern x conditioned on the previous layer's spike count can be written as

$$P(\mathbf{x}_L = x|S_{L-1} = n) = \prod_{i=1}^{N} q_n^{x(i)} (1 - q_n)^{1-x(i)}$$

$$= q_n^{\sum_i x(i)} (1 - q_n)^{N - \sum_i x(i)}, \tag{B.1}$$

where q_n represents the probability of any neuron firing given n neurons firing in the previous layer (as in equation 4.2). Then the transition probability $A_{nm} = P(S_L = m|S_{L-1} = n)$ can be computed from equation B.1 by summing over all possible combinations of patterns x such that $\sum_i x(i) = m$,

$$P(S_L = m|S_{L-1} = n) = \binom{N}{m} q_n^m (1 - q_n)^{N-m},$$
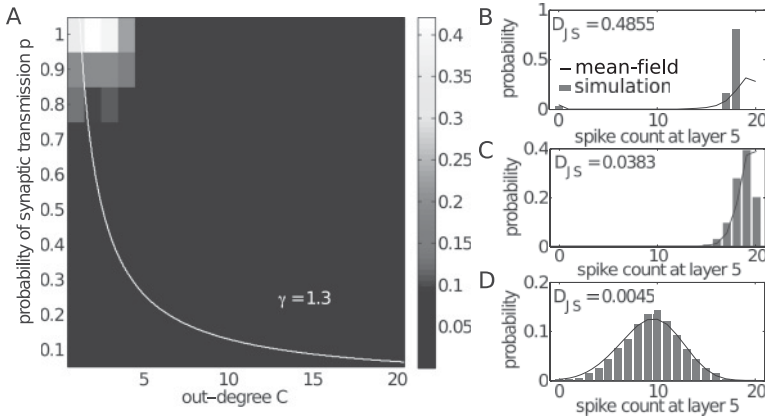
which is exactly equation 4.1.

Figure 10: Investigating the validity of the mean-field model. (A) Average JS divergence between the distribution after simulation through five layers and that predicted by the mean-field model for varying C, p. The mean-field model breaks down in the sparse limit of small C and high p. The white curve represents $\gamma = \gamma_{\text{eig}} \approx 1.3$. (B–D) Example spike count distributions from 1000 Monte Carlo simulations (gray bars) and their mean-field predictions (black line) for three orders of magnitude of the JS divergence. Parameters are (B) $C = 3$, $p = 1$, $S = 3$ for the worst fit, (C) $C = 6$, $p = 0.5$, $S = 9$ for the intermediate fit, and (D) $C = 5$, $p = 0.26$, $S = 11$ for the best fit.

Appendix C: Validity of the Mean-Field Markov Chain Model _____

In this section we investigate the validity of the mean-field Markov chain model. Specifically, for a fixed network connectivity structure, we first estimate the true spike count distribution P_5 in response to input rate S through Monte Carlo simulation. We then compare this to the distribution predicted by the mean-field Markov chain $P_5^{\text{MF}} = P_{\text{input}} A^4$ by computing the Jensen-Shannon divergence between these two distributions. Finally, we average the JS divergence (see equation 5.1) over 100 instantiations of all possible input rates and 20 random networks for that particular C and p.

Overall, the mean-field distribution approximates the true spike count distribution quite accurately, as shown in Figure 10A. The white curve overlaid on the figure indicates the level set $\gamma = \gamma_{\text{eig}}$. Note that agreement is perfect for fully connected networks. The only major challenge to the accuracy of the mean-field approximation is in the limit of low C and high p. Since C is low, there are few trials for the stochastic synapses, and the high p additionally ensures that over repetitions of the same stimulus S, the activity follows a nearly deterministic trajectory, resulting in P_5 having a narrower distribution than the mean-field predicts. Example histograms

are shown in Figures 10B–10D to give an interpretation of values for the JS divergence.

When repeated for $\theta = 7$ (data not shown), the mean-field model even better captured the true distributions, with a maximal JS divergence of 0.15 in the region of inaccuracy in the limit of $p \approx 1$ and $C \approx \gamma_{\text{obs}}$. As a final check, we also compared the means of the response distributions and found that, as expected, the averaged error was below machine epsilon (results not shown).

Appendix D: Analytical Results for the Eigenstructure of the Mean-Field Transition Matrix

Proposition 1. *For any threshold $\theta \geq 1$ and connectivity $0 < \gamma < N$, the transition matrix A possesses a unique stationary state $\pi = v_{\text{off}}$ such that $\pi A = \pi$.*

Proof. Let $\pi = (p_0, \ldots, p_N)$. Then from direct matrix multiplication with equation 4.1, the mth component of the vector πA is

$$(\pi A)_m = \sum_{n=0}^{N} p_n \binom{N}{m} q_n^m (1 - q_n)^{N-m}.$$

The stationary state requires $p_m = (Ap)_m$ for all m, that is,

$$p_m = \sum_{n=0}^{N} p_n \binom{N}{m} q_n^m (1 - q_n)^{N-m}$$

for all $m = 0, \ldots, N$. In particular, when $m = 0$, this becomes

$$p_0 = p_0 + \sum_{n=1}^{N} p_n \binom{N}{0} q_n^0 (1 - q_n)^N.$$

The summed term on the right-hand side must be zero. However, note that each of the components of this sum is nonnegative, so each must be zero, that is, for each $n = 1, \ldots, N$ either $p_n = 0$ or $(1 - q_n)^N = 0$. We could have $(1 - q_n)^N = 0$ for a particular n if $q_n = 1$. However, q_n can never be 1 for sensible parameter values of $\theta > 0$ and $0 < \gamma < N$. Therefore, we must have $p_n = 0$ for all $n = 1, \ldots, N$, and thus $p_0 = 1$. The resulting stationary state is therefore unique and precisely equal to v_{off}.

Proposition 2. *Suppose the eigenvectors of A have limits as $\gamma \to N$. Then A has an eigenvalue $\lambda^* \to 1$ as $\gamma \to N$ with corresponding eigenvector v^* that converges to a vector in the span of v_{on} and v_{off}.*

Proof. First consider (following equation 4.2),

$$q_n = 1 - \sum_{k=0}^{\theta-1} \binom{n}{k} \left(\frac{\gamma}{N}\right)^k \left(1 - \frac{\gamma}{N}\right)^{n-k}$$

as $\gamma \to N$. For $n \le \theta$, $q_n = 0$ by definition. For $n > \theta$, the sum on the right side of this equation approaches 0 since $n > k$, so $q_n \to 1$. Below we summarize for various m and n the limit of $q_n^m (1 - q_n)^{N-m}$ as $\gamma \to N$:

$$
\begin{aligned}
n > \theta: \quad & m = 0: \quad && q_n^0 (1 - q_n)^N \to 0 \\
& 0 < m < N: \quad && q_n^m (1 - q_n)^{N-m} \to 0 \\
& m = N: \quad && q_n^N (1 - q_n)^0 \to 1 \\
n \le \theta: \quad & m = 0: \quad && q_n^0 (1 - q_n)^N \to 1 \\
& 0 < m < N: \quad && q_n^m (1 - q_n)^{N-m} \to 0 \\
& m = N: \quad && q_n^N (1 - q_n)^0 \to 0.
\end{aligned}
$$

Now suppose λ is an eigenvalue of A with corresponding eigenvector v for some γ. Then λ and v satisfy

$$\sum_{n=0}^{N} v_n \binom{N}{m} q_n^m (1 - q_n)^{N-m} = \lambda v_m$$

for all $m = 0, \ldots, N$. In particular, for $m = 0$, we have

$$\sum_{n=0}^{\theta} v_n \binom{N}{0} q_n^0 (1 - q_n)^N + \sum_{n=\theta+1}^{N} v_n \binom{N}{0} q_n^0 (1 - q_n)^N = \lambda v_0,$$

which, taking $\gamma \to N$, reduces to

$$\sum_{n=0}^{\theta} \tilde{v}_n = \tilde{\lambda} \tilde{v}_0,$$

all other terms having vanished. Here, $\tilde{v}$ is the limit of v, which exists by assumption, and $\tilde{\lambda}$ is the limit of λ, which exists by the continuity of eigenvalues. For $m = N$, a similar expression is obtained:

$$\sum_{n=\theta+1}^{N} \tilde{v}_n = \tilde{\lambda} \tilde{v}_N.$$

Finally, for $0 < m < N$,

$$0 = \tilde{\lambda} \tilde{v}_m$$

This last equation reveals two possibilities: either $\tilde{\lambda} = 0$ or $\tilde{v}_m = 0$ for $0 < m < N$. The latter case implies that $\lambda = 1$; thus, the second largest eigenvalue of A converges to 1 with limiting eigenvector in the span of v_{on} and v_{off}. All other eigenvalues converge to 0.

Proposition 3.   *Suppose $N_E - N_I > \theta$. Then the (four-dimensional) transition matrix A_{in} has a unique (two-dimensional) stationary state π corresponding to no inhibitory and no excitatory neurons spiking at a layer. Moreover, the second largest eigenvalue converges to 1, and assuming the eigenvectors of A_{in} have limits as $\gamma \to N = N_E + N_I$, then its corresponding eigenvector converges to the space spanned by the vector corresponding to all inhibitory and excitatory neurons firing, and the vector corresponding to all inhibitory and excitatory neurons being quiescent.*

Proof.   Because of the structure of A_{in}, this proposition follows similarly to those of the previous two propositions.

Appendix E: Verification of Scaling Argument for the Robustness of γ in Excitatory-Inhibitory Networks

Section 7 explains that an added inhibitory population increases the robustness of optimal propagation to perturbations in γ by arguing that the net synaptic input to each neuron is scaled by a factor of $(N_E - N_I)/N$. This scaling argument is exact in the limit of large N (minimizing fluctuation in synaptic inputs) and treats only perturbations near the critical γ that give optimal rate propagation (as measured by the spike count JS divergence). The value of this critical γ, as well as the minimal value of the spike count JS divergence, need not be the same with and without inhibition under the scaling argument.

   To verify that this is the case numerically, we calculated the spike count JS divergence for two networks: the purely excitatory network (E) with $N_E = 200$ and the excitatory-inhibitory network (EI) with $N_E = 200$, $N_I = 50$. We then scaled each curve horizontally by a factor of $(N_E - N_I)/N$ (this is the identity transformation in the case of the E network) and translated the curves both vertically and horizontally to match their minimal values. If our scaling argument is correct, these curves should overlap near the minimal value. This is exactly what is seen in simulations (see Figure 11, compare with the unscaled curve for the EI network).
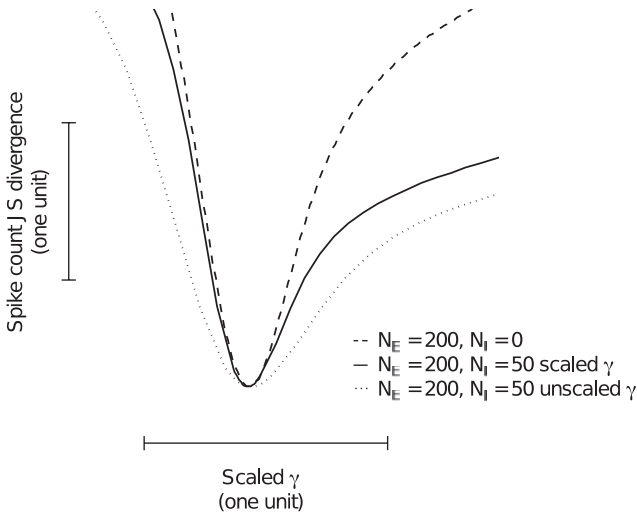
Figure 11: Spike count JS divergence of E networks with $N_E = 200$ (dashed curve) and EI networks with $N_E = 200$, $N_I = 50$ (solid curve) plotted against scaled connectivity $1/N(N_E - N_I)\gamma$. All curves have been translated horizontally and vertically to align the minimum at the same value. Note that near the minimum, the E network and the scaled EI network overlap. Compare with the spike count JS divergence for EI networks plotted against unscaled γ (dotted curve).

Appendix F: Another Metric for Rate Propagation

In addition to the measures described in the main text, we also considered the metric for rate propagation following van Rossum et al. (2002). Define the rate dissimilarity between the input rate S/N and the rate at the Lth layer S_L/N via

$$\text{RD}(\gamma, \theta) = \mathbb{E}_S[\mathbb{E}_{\text{trials}}[(S_L/N - S/N)^2 | S]]. \tag{F.1}$$

There are two potential sources of poor performance according this quantification: if the mean value of S_L is far from S or if S_L has large variance. As we see in Figure 12A, when $\theta = 1$, the rate dissimilarity reaches its minimal value at critical connectivity $\gamma_{\text{eig}} \approx \gamma_{\text{obs}}$, suggesting that for low-threshold neurons, these networks are best able to propagate rates through the network. Outside of this intermediate connectivity range, the dissimilarity between input and output returns to high values.

When the threshold is raised, the dissimilarity curve changes shape and no longer has a sharp minimum at γ_{eig} (see Figure 12C); instead, there
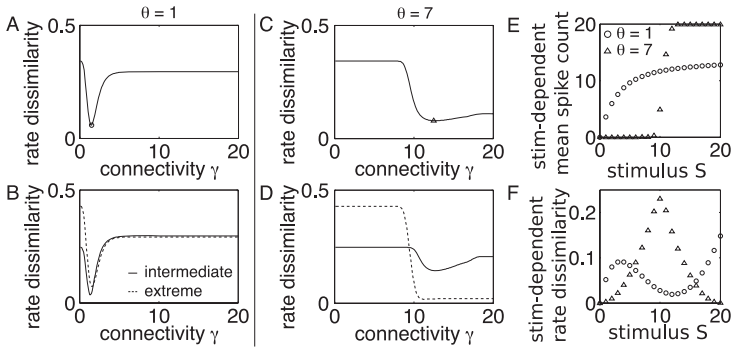
Figure 12: Rate dissimilarity for (A, B) $\theta = 1$, and (C, D) $\theta = 7$. (A, C) Rate dissimilarity plotted as a function of connectivity level γ. For (A) low-threshold networks, rate propagation is optimal at γ_{obs}. For (C) high-threshold networks, this is no longer the case. (B, D) Rate dissimilarity averaged over intermediate values ($S = 6, \ldots, 15$, solid line) and extreme rates ($S = 0, \ldots, 5$ and $16, \ldots, 20$, dashed line). (E) Mean of spike count and (F) rate dissimilarity for high-threshold (triangles) and low-threshold (circles) networks plotted as a function of input stimulus. The networks shown in panels E and F are those that minimize the stimulus-averaged rate dissimilarity, as indicated by the markers in panels A and C.

is a robust minimum. Moreover, the minimal rate dissimilarity values for the low- and high-threshold networks are at comparable values. This may at first seem surprising, given that the high-threshold networks produce strong synchrony, and this should lead to a large response variance. What is actually happening is an effect of both the increasing nullity of A and averaging over all stimuli. In Figure 12E, the stimulus-dependent mean of the output at the fifth layer is plotted as a function of the stimulus for the networks that minimize average rate dissimilarity, indicated by the markers in Figures 12A and 12C for both $\theta = 1$ (circles) and $\theta = 7$ (triangles). It is immediately clear that the low-threshold network better propagates intermediate rates as compared to the high-threshold network. By calculating the stimulus-dependent rate dissimilarity rather than taking the uniform average, we see in Figure 12F the difference between these two networks. While high-threshold networks can propagate low and high rates better than low-threshold networks, only the latter can propagate intermediate rates. This is because high-threshold networks produce bimodal responses at the connectivity value required to propagate rates. To make this point more apparent, in Figures 12B and 12C, we have crudely separated the rate dissimilarity averaged over intermediate rates (solid lines) and extreme (either high or low) rates (dashed lines). This reveals that low-threshold networks perform better than high-threshold networks for intermediate rates.

Faced with the subtlety of these results, in the main text we use the spike count JS divergence in order to unambiguously reveal network properties that support the propagation of asynchronous input distributions.

References

Abeles, M., Bergman, H., Margalit, E., & Vaadia, E. (1993). Spatiotemporal firing patterns in the frontal cortex of behaving monkeys. *Journal of Neurophysiology*, *70*, 1629–1638.

Amari, S., Nakahara, H., Wu, S., & Sakai, Y. (2003). Synchronous firing and higher-order interactions in the neuron pool. *Neural Computation*, *15*, 127–142.

Beggs, J., & Plenz, D. (2003). Neuronal avalanches in neocortical circuits. *Journal of Neuroscience*, *23*, 11167–11177.

Bertschinger, N., & Natschlager, T. (2004). Real-time computation at the edge of chaos in recurrent neural networks. *Neural Computation*, *16*, 1413–1436.

Braitenberg, V., & Schüz, A. (1998). *Cortex: Statistics and geometry of neuronal connectivity*. Berlin: Springer.

Diesmann, M., Gewaltig, M., & Aertsen, A. (1999). Stable propagation of synchronous spiking in cortical neural networks. *Nature*, *402*, 529–533.

Gabernet, L., Jadhav, S. P., Feldman, D. E., Carandini, M., & Scanziani, M. (2005). Somatosensory integration controlled by dynamic thalamocortical feed-forward inhibition. *Neuron*, *48*, 315–327.

Ganguli, S., Huh, D., & Sompolinsky, H. (2008). Memory traces in dynamical systems. *Proceedings of the National Academy of Sciences USA*, *105*, 18970–18975.

Ganmor, E., Segev, R., & Schneidman, E. (2011). Sparse low-order interaction network underlies a highly correlated and learnable population code. *Proceedings of the National Academy of Sciences USA*, *108*, 9679–9684.

Hahn, G., Petermann, T., Havenith, M., Yu, S., Plenz, D., Singer, W., et al. (2010). Neuronal avalanches in spontaneous activity in vivo. *Journal of Neurophysiology*, *104*, 3312–3322.

Hennig, M. H., Adams, C., Willshaw, D., & Sernagor, E. (2009). Early-stage waves in the retinal network emerge close to a critical state transition between local and global functional connectivity. *Journal of Neuroscience*, *29*, 1077–1086.

Jaynes, E. T. (1957). Information theory and statistical mechanics. *Physical Review*, *106*, 620–630.

Kitzbichler, M. G., Smith, M. L., Christensen, S. R., & Bullmore, E. (2009). Broadband criticality of human brain network synchronization. *PLoS Computational Biology*, *5*(3), e1000314.

Kremkow, J., Perrinet, L. U., Masson, G. S., & Aertsen, A. (2010). Functional consequences of correlated excitatory and inhibitory conductances in cortical networks. *Journal of Computational Neuroscience*, *28*, 579–594.

Kumar, A., Rotter, S., & Aertsen, A. (2008). Conditions for propagating synchronous spiking and asynchronous firing rates in a cortical network model. *Journal of Neuroscience*, *28*, 5268–5280.

Kumar, A., Rotter, S., & Aertsen, A. (2010). Spiking activity propagation in neuronal networks: Reconciling different perspectives on neural coding. *Nature Reviews Neuroscience*, *11*, 615–627.

Legenstein, R., & Maass, W. (2007). What makes a dynamical system computationally powerful? In S. Haykin, J. C. Principe, T. J. Sejnowski, & J. G. McWhirter (Eds.), *New directions in statistical signal processing: From systems to brains* (pp. 127–154). Cambridge, MA: MIT Press.

Lim, S., & Goldman, M. (2012). Noise tolerance of attractor and feedforward memory models. *Neural Computation*, *24*, 332–390.

Litvak, V., Sompolinsky, H., Segev, I., & Abeles, M. (2003). On the transmission of rate code in long feedforward networks with excitatory-inhibitory balance. *Journal of Neuroscience*, *23*, 3006–3015.

Longtin, A. (1993). Stochastic resonance in neuron models. *Journal of Statistical Physics*, *70*, 309–327.

Macke, J., Opper, M., & Bethge, M. (2011). Common input explains higher-order correlations and entropy in a simple model of neural population activity. *Physical Review Letters*, *106*(20), 208102.

Martignon, L., Deco, G., Laskey, K., Diamond, M., Freiwald, W., & Vaadia, E. (2000). Neural coding: higher-order temporal patterns in the neurostatistics of cell assemblies. *Neural Computation*, *12*, 2621–2653.

McCulloch, W. S., & Pitts, W. H. (1943). A logical calculus of the ideas immanent in nervous activity. *Bulletin of Mathematical Biophysics*, *7*, 115–133.

McDonnell, M., & Abbott, D. (2009). What is stochastic resonance? Definitions, misconceptions, debates, and its relevance to biology. *PLoS Computational Biology*, *5*(5), e1000348.

Montani, F., Ince, R. A. A., Senatore, R., Arabzadeh, E., Diamond, M. E., & Panzeri, S. (2009). The impact of high-order interactions on the rate of synchronous discharge and information transmission in somatosensory cortex. *Philosophical Transactions of the Royal Society A: Mathematical, Physical and Engineering Sciences*, *367*(1901), 3297–3310.

Mora, T., & Bialek, W. (2011). Are biological systems poised at criticality? *Journal of Statisitical Physics*, *144*, 268–302.

Nowotny, T., & Huerta, R. (2003). Explaining synchrony in feed-forward networks. *Biological Cybernetics*, *89*, 237–241.

Ohiorhenuan, I. E., Mechler, F., Purpura, K. P., Schmid, A. M., & Victor, J. D. (2010). Sparse coding and high-order correlations in fine-scale cortical networks. *Nature*, *466*, 617–621.

Petermann, T., Thiagarajan, T. C., Lebedev, M. A., Nicolelis, M. A., Chialvo, D. R., & Plenz, D. (2009). Spontaneous cortical activity in awake monkeys composed of neuronal avalanches. *Proceedings of the National Academy of the Sciences*, *106*(37), 15921–15926.

Reyes, A. (2003). Synchrony-dependent propagation of firing rate in iteratively constructed networks in vitro. *Nature Neuroscience*, *6*, 593–599.

Rosenbaum, R., Trousdale, J., & Josic, K. (2010). Pooling and correlated neural activity. *Frontiers in Computational Neuroscience*, *4*(9). doi:10.3389/fncom.2010.00009

Schneidman, E., Berry, M., Segev, R., & Bialek, W. (2006). Weak pairwise correlations imply strongly correlated network states in a neural population. *Nature*, *440*, 1007–1012.

Shlens, J., Field, G. D., Gauthier, J. L., Grivich, M. I., Petrusca, D., Sher, A., et al. (2006). The structure of multi-neuron firing patterns in primate retina. *Journal of Neuroscience*, *26*, 8254–8266.

Staude, B., Rotter, S., & Grün, S. (2010). CuBIC: Cumulant based inference of higher-order correlations in massively parallel spike trains. *Journal of Computational Neuroscience*, *29*, 327–350.

Staude, B., Grün, S., & Rotter, S. (2010). Higher-order correlations and cumulants. In S. Grün & S. Rotter (Eds.), *Analysis of parallel spike trains* (pp. 253–280). New York: Springer.

Tetzlaff, T., Geisel, T., & Diesmann, M. (2002). The ground state of cortical feedforward networks. *Neurocomputing*, *44–46*, 673–678.

Toyoizumi, T. (2012). Nearly extensive sequential memory lifetime achieved by coupled nonlinear neurons. *Neural Computation*, *24*, 2678–2699.

Trefethen, L. N., & Embree, N. (2005). *Spectra and pseudospectra: The behavior of nonnormal matrices and operators*. Princeton, NJ: Princeton University Press.

van Rossum, M., Turrigiano, G., & Nelson, S. (2002). Fast propagation of firing rates through layered networks of noisy neurons. *Journal of Neuroscience*, *22*, 1956–1966.

Vogels, T., & Abbott, L. F. (2005). Signal propagation and logic gating in networks of integrate-and-fire neurons. *Journal of Neuroscience*, *25*(46), 10786–10795.

Yu, S., Yang, H., Nakahara, H., Santos, G., Nikolic, D., & Plenz, D. (2011). Higher-order interactions characterized in cortical activity. *Journal of Neuroscience*, *31*, 17514–17526.

———————————————